Research Square

Preprints are preliminary reports that have not undergone peer review.
They should not be considered conclusive, used to inform clinical practice,
or referenced by the media as validated information.

# Nonlinear Flow Behaviour in Connected Fractures: Experimental and Numerical Investigations

**Mingwei Chen**
UNSW Sydney
**Chengguo Zhang**
chengguo.zhang@unsw.edu.au

UNSW Sydney
**Ismet Canbulat**
UNSW Sydney
**Serkan Saydam**
UNSW Sydney

**Article**

**Keywords:** Fracture network, Connected fractures, Fracture flow, Cubic law, Nonlinear flow behaviour, Governing equation

**Posted Date:** February 26th, 2026

**DOI:** https://doi.org/10.21203/rs.3.rs-8904821/v1

**License:** This work is licensed under a Creative Commons Attribution 4.0 International License. Read Full License

**Additional Declarations:** No competing interests reported.

## Abstract

Fluid flow through fractured rock masses is predominantly governed by connected fracture networks, in which intersections may play a critical role in controlling flow redistribution and energy dissipation. However, the emergence of nonlinear flow and its governing mechanisms at the network scale remain insufficiently quantified. This study investigates nonlinear flow behaviour in connected pathways by integrating fracture geometry characterisation, laboratory experiments, and numerical modelling. Borehole-derived fracture statistics are used to constrain representative intersection geometries, apertures, and spacings. Laboratory flow tests reveal a transition from effective mixing at low flow rates to interface-dominated separation at higher flow rates, with the degree of flow redistribution dependent on intersection geometry. Numerical simulations demonstrate that fracture intersections generate a confined nonlinear zone characterised by streamline curvature, vortex formation, and concentrated pressure loss, leading to pronounced deviations from linear Darcy behaviour. Parametric analyses show that cross-sectional geometry has a dominant influence on flow resistance, while a significant scale effect highlights the limitations of directly extrapolating laboratory-scale measurements to field conditions. Based on these findings, a modified cubic law (MCL) is developed by introducing a geometry-dependent exponent into the aperture term to account for interaction-induced nonlinear resistance. Validation against a fracture network model indicates that the classical cubic law overestimates flow rates by approximately 30%, whereas the proposed formulation closely reproduces Navier-Stokes solutions over a wide range of hydraulic gradients. The proposed model provides a computationally efficient and physically reliable approach for incorporating nonlinear fracture flow into network- and field-scale hydraulic analysis.


## 1 Introduction

Fluid flow through fractured rock masses plays a critical role in geological and hydrogeological systems, including groundwater circulation, geothermal reservoirs, and subsurface fluid transport [1–3]. In such systems, fluid flow is often governed by fracture networks rather than by seepage through the intact rock matrix. When fractures are highly interconnected, they form preferential pathways that enhance bulk permeability and affect flow regimes. Intersections within these connected fracture networks further complicate flow behaviour by inducing localised pressure losses, velocity redistribution, and flow separation, which may result in pronounced deviations from classical linear flow assumptions [4,5].

In connected fracture systems, intersections are key structural elements that determine network connectivity and organise flow paths, acting as “links” that enable fluid transfer between individual fractures [6,7]. Their influence on flow behaviour is manifested through several mechanisms. One important phenomenon is intersection flow localisation, where fluid velocity becomes concentrated along the intersection lineament relative to the adjacent fracture planes. Kottwitz, et al. [8] showed that when an intersection is aligned with the principal flow direction, it behaves analogously to a high-conductivity conduit and provides a preferential flow pathway. The number and spatial distribution of intersections also determine whether a fracture network reaches the percolation threshold, defined as the critical condition under which fractures form a continuous flow network. Ozkaya and Mattner [9] reported that when the average number of intersections per fracture ( $\lambda$ ) is between 1 and 2, fractures form small clusters within limited influence on large-scale flow, whereas for $\lambda$ ≥2, clusters interact exponentially to produce extensive connected channels. Huang, et al. [10] demonstrated that fractures remain hydraulically isolated and contribute negligibly to macroscopic flow in the absence of interconnections. Similarly, Zhang, et al. [11] showed that fractures with only one intersection behave as “dead ends” and generally do not sustain steady-state flow. Li, et al. [12] revealed that intersections promote the formation of interconnected fracture clusters, among which a single well-connected cluster containing a large proportion of fractures may dominate the total network flow.

Beyond the structural influence, intersections also govern local hydrodynamics by acting as converge points for fluids originating from different pathways. Two conceptual models have been developed to describe transport behaviour at intersections: complete mixing, which assumes that all incoming fluids and solutes mix fully within the intersection before exiting [13,14], and streamline routing, which assumes that fluids pass through the intersection along distinct streamlines with minimal mixing [6,15,16]. Although these local mixing rules affect solute redistribution, previous studies suggest that the geometric features of fracture networks, particularly the arrangement and connectivity of intersections, exert a stronger control

on network-scale transport than the specific mixing model adopted [6]. Moreover, intersections may introduce hydraulic constrictions, defined as the minimum wall-to-wall distance at the plane where two fractures meet [17,18]. When such constrictions are significantly smaller than the apertures of the adjoining fractures, they generate strong velocity contrasts and localised energy losses, thereby enhancing nonlinear flow effects. In extreme cases, steep pressure gradients near intersections may even induce local flow reversal relative to the global pressure gradient [7,19,20].

Despite substantial progress in experimental, analytical, and numerical investigations, fluid flow through interconnected fracture networks remains inadequately understood. Although nonlinear and non-Darcian flow behaviour has been examined in individual fractures, its emergence and governing mechanisms at the network scale remain constrained. The influence of fracture intersections on flow partitioning, local pressure losses, and energy dissipation has received limited quantitative assessments. In this context, this paper combines laboratory experiments and high-resolution numerical modelling to investigate nonlinear flow in connected pathways with varying apertures and intersection angles. Flow interaction mechanisms are analysed in terms of velocity fields, pressure losses, and vortex formation. A modified cubic law is developed to describe the relationship between hydraulic gradient and flow rate under nonlinear conditions. This study is expected to improve the quantitative representation of intersection-controlled nonlinear flow and to provide a governing equation suitable for network- and field-scale analyses.

## 2 Fracture geometry characterisation

Field data associated with rock fracture characteristics were compiled from documented cases of mining and tunnelling in New South Wales, Australia [21,22], yielding a total of 277 datasets, as illustrated in Fig. 1(a). These data are analysed to derive statistically representative descriptions of fracture orientation, aperture, and spacing. The resulting parameter ranges and characteristic values are then used to guide the design of connected flow chambers and the specification of boundary conditions for laboratory fluid flow experiments, thereby ensuring consistency between the experimental configuration and the fracture systems observed in the field.

# 2.1 Fracture orientation

Fracture orientation describes the geometric direction of fractures within rock masses. In three dimensions, it is commonly defined in by strike and dip, while in two dimensions it can be represented by fracture traces projected from dip points according to dip angles [23,24]. Figure 1(a) shows fracture orientations obtained from acoustic televiewer logging in two boreholes.

Based on the dip angle distribution shown in Fig. 1(b), the fractures can be classified into low-angle and high-angle sets. Low-angle fractures, with dip angles between 0 and 17 degrees, are mainly associated with bedding plane separation caused by differential deformation between adjacent strata [25,26]. In contrast, high-angle fractures, with dip angles ranging from 67 to 90 degrees, are primarily induced by tensile failure when the applied stress exceeds the tensile strength of the rock [27].

Therefore, the dip angle pattern suggests two dominant intersection geometries within the fracture system: (1) intersections between high-angle and low-angle fractures at angles approaching 90 degrees, and (2) intersections between two high-angle fractures with crossing angles up to about 46 degrees. These representative intersection configurations are therefore incorporated into the design of flow chambers.

# 2.2 Fracture aperture

Fracture aperture refers to the separation between opposing fracture surfaces and directly controls the ability of a fracture to transmit fluids. Field-scale aperture estimates can be calculated from borehole packer tests, such as Lugeon-type measurements [28–30], as well as captured from high-resolution fracture images acquired using acoustic or optical televiewer logging [31–33].

Aperture values derived from these two independent approaches are combined to establish a statistical characterisation. As illustrated in Fig. 1(c), the interpreted apertures range from approximately 0.46 mm to 10.73 mm, with a mean value of 3.93 mm. Accordingly, an aperture of 4 mm is adopted as a representative value for the fabrication of intersected flow chambers in the laboratory. To further assess the influence of aperture variability on flow behaviour, additional aperture values ranging from 1 to 10 mm are examined through numerical simulations.

## 2.3 Fracture spacing

Fracture spacing is defined as the perpendicular distance between adjacent fractures within a rock mass and represents the characteristic length scale of intact rock bounded by discontinuities. This parameter plays a critical role in influencing fracture connectivity and the formation of continuous flow pathways within a fracture network. Borehole logging data, as shown in Fig. 1(c), indicate that fractures developed within the zone exhibit spacings ranging from 0.1 and 1.0 m, with a mean value of approximately 0.2 m.

Based on the geometric characterisation, the spacing of experimental flow chambers can be designed with a length of 0.2 m, intersecting at prescribed angles of 45° and 90° at their midpoint. Under these conditions, the half-length of each flow path (approximately 0.1 m) is more than an order of magnitude greater than the representative fracture aperture, allowing the flow to stabilise before reaching the intersection region. In addition, the observed spacing also implies that individual fractures may extend laterally over widths of up to 0.2 m if they are approximated as elliptical or near-circular features in three-dimensional space. This geometric relationship ensures that the experimental setup can remain consistent with the scale and structural characteristics of field-observed fracture systems.

# 3 Laboratory experiments

Laboratory experiments were conducted to investigate fluid flow through intersected fractures under controlled fluid flow conditions. The experimental setup was designed based on the geometric parameters identified in Section 2, including intersection angles, apertures, and pathway lengths. The test system ensures stable fluid injection, accurate pressure measurement, and reliable data acquisition. This section describes the configuration of the flow chambers, experimental apparatus, and procedures implemented during the flow tests.

## 3.1 Flow chamber configuration

Flow chambers were manufactured to simulate fracture intersections with angle of 90 and 45 degrees, as shown in Fig. 2(a). These configurations represent the dominant geometries identified from the fracture orientation analysis in Section 2. Each flow pathway was designed with a length of 200 mm, a nominal aperture of 4 mm, and a width (treated as the out-of-plane depth) of 2 mm, in accordance with the representative fracture spacing and aperture values derived from field observations.

The fracture pathways were precision-machined on stainless steel plates using computer numerical control (CNC) milling, achieving a dimensional tolerance of ± 0.05 mm. This manufacturing approach ensures geometric consistency among different chambers and minimises unintended variability in aperture and pathway length. A continuous peripheral groove was also machined around the flow pathways to accommodate an O-ring cord, providing a reliable seal when the chamber was assembled and thereby preventing water leakage and air intrusion during testing. Overall, this design allows the experimental setup to reproduce key geometric features of connected fracture systems at a reduced scale, while maintaining consistency with the characteristic dimensions and spatial arrangement of measured fractures.

## 3.2 Experimental setup

The flow chambers were formed by placing an acrylic plate over the machined stainless steel plate to enclose the flow pathways, as shown in Fig. 2(b). The two plates were fixed together using 24 hexagon socket screws to prevent relative displacement and to ensure reliable sealing during testing. This configuration provides a stable flow domain while allowing visual observation of the intersection region. Four brass connectors were installed in the acrylic plate to serve as inlets and outlets. As shown in Fig. 2(c), fluid injection was supplied by two syringe pumps assembled from acrylic tubes, stepper motors

and guide rails, with several components produced by 3D printing. The pumps were operated by dedicated controllers to maintain constant injection rates. Calibration tests indicate that the flow rate error ranges from 0.05% to 0.33%, mainly due to the non-ideal circular shape of the acrylic tubes.

The pressure difference between each pair of inlet and outlet was measured using a differential pressure transducer with a minimum resolution of 0.1 kPa. The outlet flow rates were monitored by non-contact flow meters with a resolution of 20 mL/min. All signals were recorded continuously using a National Instruments data acquisition module at a sampling frequency of 100 Hz. Water at 20°C was used as the working fluid, with a density of 0.998 kg/L and a dynamic viscosity of 0.001 Pa·s. The experiments were conducted under the following assumptions: (i) the internal surfaces of the flow chambers are smooth; (ii) the pressure drop caused by flow interaction is mainly concentrated at the fracture intersection; and (iii) additional pressure losses are related to the geometry of the inlet and outlet reservoirs.

## 3.3 Experimental implementation

Single-fracture flow tests were first carried out to examine the sealing performance and operational stability of the experimental system. During these tests, the remaining flow branches were blocked using moulded resin gels, leaving only one flow pathway active. Under constant water injection, the pressure drop and flow rate were monitored simultaneously to verify that no water leakage occurred and that air did not enter the system, thereby ensuring that the measurements were not affected by external disturbance.

Based on the results of validation, the injection rates for the intersected-fracture experiments were set between 60 and 200 mL/min. To visualise flow interaction at the intersection, a low-concentration blue dye solution was injected through one inlet, while clear water was supplied through the other. Owing to the low dye concentration, its influence on fluid density and dynamic viscosity can be neglected, and the overall flow behaviour remains unchanged. During each test, the pressure difference across the flow chambers and the discharge rates at the outlets were continuously recorded, while steady flow conditions were maintained. Each experimental condition was repeated several times to reduce random error and to confirm the stability and reproducibility of the measured results, providing a consistent dataset for subsequent analysis.

# 4 Numerical modelling

A three-dimensional numerical model was established in COMSOL Multiphysics to reproduce the laboratory flow conditions and to provide a quantitative interpretation of the measured pressure drop-flow rate relationship. The model was calibrated and evaluated by comparing simulated pressured drops with those obtained from experiments at corresponding injection rates, thereby enabling further investigation of more flow scenarios that cannot be readily configured under laboratory conditions.

## 4.1 Model configuration

Single-phase incompressible flow was assumed, and the $k-\omega$ turbulence formulation was applied to account for the onset of nonlinear flow behaviour and the associated pressure losses within the intersection zone [34,35]. The computational domain was discretised using an unstructured triangular mesh. A minimum element size of 0.03 mm was selected to ensure adequate spatial resolution while maintaining reasonable computational cost. Additional mesh refinement was applied around the intersection region, where strong velocity gradients and flow interaction are expected. Specifically, a maximum element growth rate of 1.03 was imposed along the four intersection edges, and the element size at the eight corner vertices was restricted to 0.05 mm. Boundary layer meshes were introduced along the fracture walls using six layers, with a stretching factor of 1.8 and a thickness adjustment factor of 0.5, to improve the representation of near-wall flow behaviour.

Fully developed velocity profiles were prescribed at both inlets, while normal outflow conditions were assigned to the outlets. With this configuration, the model reached stationary convergence within approximately 65 minutes for each simulation case. The numerical simulations were performed over the same range of injection rates as those used in the laboratory tests.

## 4.2 Model calibration

The performance of the numerical model was evaluated by comparing simulated and measured pressure drops over a range of injection rates. Figure 3(a) to (d) presents the calibration results for the four representative configurations. For each injection rate, ten paired values of pressure drop and flow rate were obtained from repeated tests, and their mean values were used for comparison with the numerical predictions. The agreement between experimental and simulation results was quantified using the coefficient of determination ( $R^2$), calculated between the averaged experimental data and the corresponding numerical values. The results $R^2$ values for cases (a) to (d) are 0.987, 0.977, 0.978, and 0.979, respectively, indicating a consistently high level of correlation across all tested configurations.

As shown in Fig. 3, the simulated pressure drop-injection rate curves closely follow the experimental trends for both intersection angles and apertures. Minor deviations between simulated and measured values are primarily observed at higher flow rates, which is potentially attributed to strong flow interaction and increased local velocity gradients within the intersection zone. Overall, the calibration results demonstrate that the numerical model is capable of capturing the main features of nonlinear flow behaviour and pressure loss associated with intersected fractures. Therefore, the valeted model can provide a reliable basis for further numerical investigations, including the analysis of flow interaction mechanisms and the development of simplified governing relationship for connected fracture systems.

## 5 Results and discussions

# 5.1 Flow interaction at intersection

Connected-fracture flow tests were conducted with water injection rates ( $Q$) ranging from 60 to 200 mL/min. Within this range, the total pressure drop reflects both the intrinsic flow behaviour along individual pathways and the interaction between the two inflows within the intersection region. To capture potential interactions, a dilute blue dye solution was injected through inlet $I_2$, while clear water was injected through inlet $I_1$, as shown in Fig. 4. Due to its low concentration, the dye has a negligible influence on fluid density and viscosity [36,37].

For both the 90-degree and 45-degree intersection configurations, the colour distribution at the outlets varies with injection rates. As illustrated in Fig. 4, the colour at outlet $O_2$ becomes progressively lighter as the flow rate increases. At relatively low flow rates, the dyed and clear fluids mix effectively within the intersection region before the outlet branches, resulting in comparable colour intensities at $O_1$ and $O_2$. This phenomenon indicates strong mass exchange between the two inflows under low-velocity conditions. With increasing injection rates, a distinct interface develops between the dyed and clear fluids within the intersection zone. The formation of this interface limits transverse mixing and reduces mass exchange between the two inflows. As a result, part of the dyed fluid is diverted from its direct pathway ($I_2$-$O_2$) towards the alternative branch ($I_2$-$O_1$). The redistribution of discharge demonstrates that the interaction region acts as a control point for flow partitioning, and that the efficiency of fluid mixing decreases as the flow becomes faster.

Explicit differences are also observed between the two intersection geometries. For the same injection rate, the 45-degree intersection produces a lighter colour at outlet $O_2$ than the 90-degree intersection. This indicates a smaller reduction in flow velocity and a weaker redistribution on mass exchange across the intersection. In contrast, the 90-degree configuration promotes stronger separation between the two inflows, leading to a more pronounced interface and a greater redistribution of dyed fluid towards outlet $O_1$. These observations suggest that intersection angle plays an important role in governing the degree of fluid mixing and the partitioning of discharge between outlet branches.

Overall, the experimental results demonstrate that flow interaction at fracture intersections is characterised by a transition from efficient mixing at low flow rates to interface-controlled separation at higher flow rates. The development of a distinct interface supresses mass exchange between the two inflows and modifies their discharge pathways. This behaviour highlights the importance of intersection geometry and flow rate in controlling fluid redistribution within connected fracture systems, forming basis for interpreting the nonlinear pressure drop-flow rate responses observed in both experimental and numerical investigations.

## 5.2 Localised nonlinear flow behaviour

Numerical simulations were conducted to investigate the detailed flow behaviour associated with the interaction between the two inflows. The streamlines shown in Fig. 5 indicate that fluid flow remains approximately linear within the inlet branches, where viscous resistance dominates and the velocity field is relatively uniform. After entering the intersection region, however, the streamlines depart from straight trajectories and become significantly curved, indicating a transition from simple channel flow to an interaction-controlled regime governed by flow redistribution between the two pathways.

With increasing injection rates, the streamline curvature becomes more pronounced for both intersection angles, as shown in Fig. 5(a) and (c), demonstrating that flow interaction intensifies at higher velocities. Comparison between the two configurations further shows that the 45-degree intersection produces a stronger local acceleration within the intersection region than 90-degree intersection case. This results in a higher-velocity core along the interface between the two inflows and a more focused main flow path. Comparatively, the 90-degree intersection promotes greater lateral spreading of the flow and stronger deflection at the intersection.

Distinct vortex structures are consistently observed in the low-velocity zones adjacent to the main flow paths. As illustrated in Fig. 5(a) and (c), a dead zone develops in the outlet region near the intersection and is separated from the primary stream by a narrow shear interface. Across this interface, part of the high-speed flow in entrained into the stagnant region, forming a stable recirculating vortex. This recirculation acts as a local energy sink and introduces additional hydraulic resistance.

The pressure fields shown in Fig. 5(b) and (d) further characterise the hydraulic behaviour of the dead zone. For both intersection angles, the dead zone corresponds to the lowest-pressure region, reflecting weak throughflow and limited fluid exchange within the recirculating area. In contrast, relatively high pressure is concentrated near the interface between the two inflows, where flow redirection and interaction are most intense. A comparison between the two configurations indicates that the interface pressure is higher for the 90-degree intersection than for the 45-degree intersection, implying stronger obstruction and energy dissipation in the perpendicular case. The coexistence of low-pressure dead zones and high-pressure interaction regions highlights the strong spatial heterogeneity of the pressure field induced by flow interaction and explains the formation of a confined nonlinear region near the intersection.

To quantify the nonlinear behaviour, velocity and pressure were extracted along a survey line passing through the centre of the intersection, as shown in Fig. 6. In the 90-degree scenario, the flow decelerates as it approaches the intersection and reaches a minimum velocity at the centre, reflecting strong flow deflection and redistribution. However, in the 45-degree configuration, the velocity increases across the intersection, indicating partial alignment of the two inflows and enhanced throughflow along the interface. In both configurations, the velocity reaches a peak near the downstream side of the intersection and then decreases sharply within the outlet branch due to vortex-induced resistance and flow separation. This effect becomes more pronounced at higher flow rates and is particularly evident for the 90-degree intersection, where the recirculation zone has a larger fraction of the flow cross-section.

The corresponding pressure profiles shown in Fig. 6(c) and (d) exhibit an approximately linear decline along the inlet branches, followed by a concentrated pressure drop within the intersection region and a gradual recovery downstream. The localised pressure loss is primarily associated with the interaction zone rather than with frictional resistance along the straight flow paths. Increasing injection rates lead to a disproportionate increase in this local pressure drop, confirming the nonlinear nature of the interaction-induced resistance. Although the intersection angle has a relatively small influence on the overall pressure gradient for a given discharge, it significantly affects the spatial distribution of velocity and the extent of the recirculation zone.

Overall, the numerical modelling results demonstrate that flow interaction at the intersection gives rise to a confined nonlinear zone characterised by streamline curvature, vortex formation, and concentrated pressure loss. This nonlinear zone governs both the redistribution of flow between outlet branches and the additional energy dissipation reflected in the pressure drop-flow rate relationship, providing a mechanistic explanation for the experimentally observed deviation from linear Darcy behaviour.

## 5.3 Governing equation development

### 5.3.1 Pressure drop responses to cross-sectional geometries

Numerical modelling results demonstrate that, although the intersection angle has only a limited influence on the overall pressure drop, the cross-sectional geometry of connected pathways plays a dominant role in governing flow resistance. To quantify the geometric effect, a parametric study was conducted using the calibrated model by varying pathway aperture and width within ranges derived from field observations. Apertures between 2 and 10 mm and widths from 2 mm to 200 mm were taken into account, representing a progressive transition from laboratory-scale flow pathways to geometries relative to in-situ conditions.

As summarised in Table 1, the simulated pressure drop ( $\Delta p$) between the inlet and outlet exhibits two distinct trends. For a given geometry, $\Delta p$ increases monotonically with injection rates, reflecting enhanced flow interaction and vortex-induced energy dissipation within the intersection zone. Conversely, for a given injection rate, $\Delta p$ decreases with increasing pathway geometry. Based on the data, regression analysis reveals that the geometric effect follows an explicit power-law relationship, as shown in Table 1, with the exponent increasing from approximately 1.73 to 2.07 as the injection rate increases. Similarly, Table 2 shows that $\Delta p$ decreases with pathway width according to a power-law function, with the corresponding exponent increasing from 1.37 to 1.51. These fitted relationships provide a quantitative description of the nonlinear geometric effect on pressure losses and are consistent with classical concepts of hydraulic resistance expressed in the Darcy-Weisbach formulation.

A pronounced scale effect is further observed by upscaling the pathway width from 2 mm to 200 mm. As shown in Table 2, $\Delta p$ reduces by nearly three orders of magnitude to only about 0.2% of its laboratory-scale value. This substantial reduction demonstrates that pressure losses measured in small-scale flow chambers cannot be directly extrapolated to natural fracture systems without accounting for geometric scaling effects.

Table 1

Pressure drop ($\Delta p$) under different pathway apertures ($a$) and injection rates ($Q$)

| $Q$ | $\Delta p$ (Pa) | | | | | | | | | | Relationship |
|---|---|---|---|---|---|---|---|---|---|---|---|
| mL/min | *a* = 1 mm | *a* = 2 mm | *a* = 3 mm | *a* = 4 mm | *a* = 5 mm | *a* = 6 mm | *a* = 7 mm | *a* = 8 mm | *a* = 9 mm | *a* = 10 mm | $\Delta p =$ |
| 60 | 2025.3 | 415.4 | 191.7 | 115.3 | 85.2 | 65.7 | 53.4 | 44.9 | 38.6 | 33.8 | $1536.5a^{-1.73}$ |
| 120 | 5555.3 | 1125.5 | 494.7 | 289.4 | 197.4 | 148.6 | 119.5 | 99.6 | 84.9 | 73.7 | $4379.9a^{-1.85}$ |
| 180 | 10216.7 | 2108.7 | 919.8 | 530.4 | 354.3 | 257.4 | 200.3 | 165.1 | 126.1 | 117.2 | $8582.5a^{-1.93}$ |
| 240 | 17423.8 | 2801.8 | 1367.5 | 805.6 | 566.6 | 328.0 | 289.8 | 240.1 | 184.1 | 168.2 | $13476a^{-1.98}$ |
| 300 | 24823.8 | 4001.8 | 2007.5 | 1155.6 | 806.6 | 458.0 | 401.8 | 325.1 | 250.1 | 225.2 | $19743a^{-2.01}$ |
| 360 | 33423.8 | 5401.8 | 2767.5 | 1565.6 | 1086.6 | 608.0 | 529.8 | 420.1 | 324.1 | 288.2 | $27197a^{-2.03}$ |
| 420 | 43223.8 | 7001.8 | 3647.5 | 2035.6 | 1406.6 | 778.0 | 673.8 | 525.1 | 406.1 | 357.2 | $35844a^{-2.05}$ |
| 480 | 54223.8 | 8801.8 | 4647.5 | 2565.6 | 1766.6 | 968.0 | 833.8 | 640.1 | 496.1 | 432.2 | $45692a^{-2.07}$ |

Table 2

Pressure drop ($\Delta p$) under different pathway widths ($w$) and injection rates ($Q$)

| $Q$ | $\Delta p$ (Pa) | | | | | | | | Relationship |
|---|---|---|---|---|---|---|---|---|---|
| mL/min | *w* = 2 mm | *w* = 4 mm | *w* = 10 mm | *w* = 20 mm | *w* = 40 mm | *w* = 80 mm | *w* = 140 mm | *w* = 200 mm | $\Delta p =$ |
| 60 | 131.8 | 28.1 | 5.8 | 2.4 | 1.1 | 0.5 | 0.3 | 0.2 | $198.7w^{-1.37}$ |
| 120 | 272.8 | 59.3 | 12.8 | 4.7 | 2.2 | 1.0 | 0.6 | 0.4 | $421.9w^{-1.37}$ |
| 180 | 523.4 | 115.9 | 23.0 | 8.7 | 3.7 | 1.6 | 0.9 | 0.6 | $817.2w^{-1.43}$ |
| 240 | 712.8 | 159.3 | 32.4 | 11.1 | 5.1 | 2.2 | 1.2 | 0.8 | $1191.6w^{-1.43}$ |
| 300 | 1068.6 | 240.6 | 46.4 | 17.0 | 6.9 | 2.9 | 1.6 | 1.0 | $1892.7w^{-1.47}$ |
| 360 | 1312.8 | 299.3 | 58.4 | 19.1 | 8.5 | 3.6 | 1.9 | 1.3 | $2324.8w^{-1.47}$ |
| 420 | 1672.8 | 384.3 | 73.8 | 23.7 | 10.4 | 4.3 | 2.3 | 1.5 | $3034.3w^{-1.49}$ |
| 480 | 2072.8 | 479.3 | 90.8 | 28.7 | 12.4 | 5.1 | 2.7 | 1.8 | $3842.0w^{-1.51}$ |

## 5.3.2 Flow nonlinearity characterisation

The transport of fluid through intersected pathways can be interpreted using momentum conservation for incompressible viscous media. In a general vector form, the governing relation can be expressed as

$$\rho\left(\frac{DV}{Dt}\right) = -\nabla p + \nabla \bullet \Sigma + \rho G \text{ (Eq. 1)}$$

Where $V$ represents the velocity field, $p$ is the pressure, $\Sigma$ is the viscous stress tensor, and $G$ represents the external body force per unit mass. For a Newtonian fluid with constant density and viscosity, Eq. 1 can be written as

$$\frac{\partial V}{\partial t} = \kappa \nabla^2 V - \frac{1}{\rho}\nabla p + (V \bullet \nabla) V + G \text{ (Eq. 2)}$$

Where $\kappa$ is the kinematic viscosity. The diffusion term $\kappa \nabla^2 V$ varies linearly with velocity, whereas the advection term $(V \bullet \nabla) V$ introduces a nonlinear contribution proportional to the square of velocity. This mathematical expression implies that, when strong streamline distortion and flow interaction occur at pathway intersections, hydraulic resistance cannot be adequately described by a purely linear relationship.

To characterise this behaviour at the macroscopic scale, a dimensionless hydraulic gradient $I$ is introduced:

$$I = \frac{\Delta p}{\rho g L_c} \text{ (Eq. 3)}$$

Where $\Delta p$ is the pressure difference between inlet and outlet and $L_c$ is the characteristic flow length.

Figure 7 compares linear and power-law relationships between the hydraulic gradient ( $I$) and the flow rate ( $Q$) for different apertures. The best-fit curves in Fig. 7 indicate that $I$ varies with $Q$ following a second-order polynomial:

$I = AQ + BQ^2$ (Eq. 4)

Where $A$ and $B$ are fitting coefficients. The linear term represents viscous-dominated transport, while the quadratic term represents additional resistance induced by inertial effects associated with streamline curvature, flow separation, and interaction between intersected pathways. The increasing contribution of the quadratic term demonstrates that progressively larger pressure gradients are required to sustain the same discharge under nonlinear flow conditions.

For comparison, laminar flow between parallel smooth plates is commonly approximated by the classical cubic law:

$Q = \frac{\rho\, g}{12\mu} a^3 I$ (Eq. 5)

Where $a$ is the aperture and $\mu$ is the dynamic viscosity. As shown in Fig. 7, the linear representation systematically overestimates the discharge for a given hydraulic gradient because it neglects flow separation, vortex formation, and energy dissipation induced by pathway intersections.

To account for these effects, a generalised scaling form is proposed:

$Q = \frac{\rho\, g}{12\mu} \Gamma\, a^{\xi}\, I$ (Eq. 6)

Where $\Gamma$ and $\xi$ are geometry-dependent parameters determined by regression analysis. For the smallest aperture, the optimal fit yields $\Gamma \approx 1$ and $\xi > 3$, indicating a super-cubic correlation between discharge and aperture. Extending this analysis to apertures ranging from 2 to 10 mm gives the results summarised in Table 3.

Table 3

Values of $\Gamma$ and $\xi$.

| **Aperture (mm)** | $\xi$ | $\Gamma$ |
|---|---|---|
| 1 | 3.277 | 0.996 |
| 2 | 3.371 | 0.993 |
| 3 | 3.460 | 0.992 |
| 4 | 3.509 | 0.990 |
| 5 | 3.570 | 0.990 |
| 6 | 3.612 | 0.988 |
| 7 | 3.659 | 0.987 |
| 8 | 3.676 | 0.985 |
| 9 | 3.688 | 0.984 |
| 10 | 3.699 | 0.983 |

Further regression analysis on the values of $\Gamma$ and $\xi$ yield

$\xi = 3.772 - 0.625 \times 0.797^{a}$ (Eq. 7)

$\Gamma = 0.996 - 0.001a$ (Eq. 8)

with $R^2$ of 0.997 and 0.985, respectively. Eq. 7 indicates that the exponent $\xi$ increases asymptotically with aperture, ranging from 3.147 to 3.772. This trend suggests that deviations from cubic scaling persist even for relatively large openings, reflecting

the sustained influence of nonlinear resistance mechanisms induced by flow interaction. In contrast, variations in $\Gamma$ remain negligible and may be approximated as unity over the investigated aperture range.

Substituting Eqs. 7 and 8 into Eq. 6 yields a modified cubic law:

$Q = \frac{\rho\, g}{12\mu} a^{3.772-0.625\times\, 0.797^{a}} I$ (Eq. 9)

Eq. 9 incorporates the effects of flow interaction and inertial dissipation into a compact constitutive form. Compared with the classical cubic law, this expression provides an improved description of hydraulic behaviour in intersected pathways by embedding the geometric control on nonlinear resistance into the aperture exponent.

### 5.3.3 Governing equation validation

A fracture network was established in COMSOL to validate the reliability of the proposed modified cubic law (MCL) and to evaluate its performance against the full Navier-Stokes (N-S) solution, following the fracture network configuration reported by Liu, et al. [37]. The model domain is 1×1 m and consists of 15 fractures and 27 intersections, as illustrated in Fig. 8(a). Four inlets were prescribed on the left boundary using a higher pressure head, and five outlets were prescribed on the right boundary using zero pressure head. The top and bottom boundaries were treated as impermeable. Different apertures were assigned to the 15 fractures according to the network morphology. To accurately resolve flow heterogeneity and local interaction effects, the fractures were discretised using an extremely fine mesh. Water was used as the fluid, with physical properties specified under standard temperature and pressure conditions. In addition, blocky entities separated by the fractures were assumed to be impermeable.

The MCL formulation (Eq. 9) was implemented in COMSOL through a user-defined permeability function applied along each fracture, with parameters determined from the fracture-specific aperture and the exponent derived from Eq. 7. Fluid flow analysis was first conducted under a hydraulic gradient of $1\times10^{-5}$, and the resulting fluid pressure and flow velocity fields are shown in Fig. 8(b) and (c), respectively. The results indicate that pronounced flow localisation and velocity heterogeneity can be observed among different fractures, highlighting the nonlinear interaction effects captured by the MCL.

Subsequent fluid flow analyses were conducted by progressively increasing the hydraulic gradient to assess the robustness of the MCL relative to the conventional cubic law and the full N-S solution, as summarised in Fig. 8(d). The results show that, for a given hydraulic gradient, the cubic law systematically overestimates the flow rate by approximately 30%, potentially due to its neglect of nonlinear effects induced by fracture intersections and velocity redistribution. In contrast, the MCL yields substantially improved predictions, achieving an $R^2$ of 0.99 relative to the N-S solution for hydraulic gradients up to $1\times10^{-3}$. This agreement demonstrates the capability of the MCL to represent super-cubic aperture dependence and the influence of geometric heterogeneity within interconnected fracture networks.

Beyond this range, however, the MCL tends to underestimate the flow rate under a fixed gradient, which is likely attributed to enhanced inertial contributions and weak turbulence effects that are not explicitly represented in the semi-empirical formulation. Nevertheless, the MCL effectively bridges the gap between the conventional cubic law assumption and the full N-S solution, providing a computationally efficient yet accurate approach for modelling fluid flow in fracture networks. Moreover, the proposed approach offers a practical basis for extending semi-empirical fluid flow analysis to field-scale models, facilitating the incorporation of nonlinear fracture flow behaviour into hydrogeological and reservoir-scale simulations.

## 6 Conclusions

This study investigated nonlinear fluid flow in connected fractures by integrating laboratory experiments and numerical modelling. Field data were collected to identify representative fracture geometries, apertures, and spacings. Laboratory flow tests with dye visualisation showed that fracture intersection acts as key control of flow partitioning and mixing, with a transition from effective mixing at low flow rates to separation at higher flow rates. This behaviour is dependent on intersection geometry, with perpendicular intersections producing more pronounced flow deflection than oblique configurations.

Numerical simulations revealed that intersections generate a confined nonlinear zone characterised by streamline curvature, vortex formation, and concentrated pressure loss. Within this zone, hydraulic resistance departs from linear Darcy behaviour and is governed by interaction-induced energy dissipation. Quantitative analyses indicated that cross-sectional geometry dominates flow resistance, whereas intersection angle plays a secondary role, and a significant scale effect shows that laboratory-scale results cannot be directly extrapolated to field conditions without geometric scaling.

A modified cubic law (MCL) was developed by introducing a geometry-dependent exponent into the aperture term to account for nonlinear resistance associated with flow interaction and recirculation. Validation against a fracture network model showed that the classical cubic law overestimates flow rates by 30%, whereas the MCL closely reproduces the Navier-Stokes solution ( $R^2 \approx 0.99$) for hydraulic gradient up to $1\times10^{-3}$. At higher gradients, underestimation tends to occur and reflects the increasing influence of inertial effects that are not explicitly represented in the semi-empirical formulation.

Overall, fracture intersections alter flow behaviour by inducing localised nonlinear resistance and geometric control on discharge. The proposed MCL provides a compact and physically informed governing equation for fracture flow analysis, enabling efficient incorporation of nonlinear flow behaviour into network- and field-scale simulations for subsurface fluid flow analysis.

## Declarations

The authors declare that they have no known competing financial interests or personal relationships that could have appeared to influence the work reported in this paper.

# Funding declaration

The author(s) received no financial support for the research of this article.

# Author contributions

Mingwei Chen: Formal analysis, Writing - Original Draft.

Chengguo Zhang: Validation, Writing - Review & Editing.

Ismet Canbulat: Conceptualization, Supervision.

Serkan Saydam: Investigation, Supervision.

# Data availability statement

All data generated or analysed during this study are included in this published article.

## References

1. Mountassir, G. E., Lunn, R. J., Moir, H. & MacLachlan, E. Hydrodynamic coupling in microbially mediated fracture mineralization: formation of self-organized groundwater flow channels. *Water Resour. Res.* **50**, 1–16. https://doi.org/10.1002/2013WR013578 (2014).
2. Mayo, A. L. & Koontz, W. Fracture flow and groundwater compartmentalization in the rollins sandstone, Lower Mesaverde Group, Colorado, USA. *Hydrogeol. J.* **8**, 430–446. https://doi.org/10.1007/s100400000056 (2000).
3. Fu, P., Hao, Y., Walsh, S. D. C. & Carrigan, C. R. Thermal drawdown-induced flow channeling in fractured geothermal reservoirs. *Rock. Mech. Rock. Eng.* **49**, 1001–1024. https://doi.org/10.1007/s00603-015-0776-0 (2016).

4. Bui, C. M. & Matthai, S. K. Influence of fluid dynamics on flow and transport in natural fracture networks. *Comput. GeoSci.* **29**, 23. https://doi.org/10.1007/s10596-025-10361-x (2025).
5. Wood, T. R., Nicholl, M. J. & Glass, R. J. Influence of fracture intersections under unsaturated, low-flow conditions. *Water Resour. Res.* **41** https://doi.org/10.1029/2004WR003281 (2005).
6. Berkowitz, B. Characterizing flow and transport in fractured geological media: A review. *Adv. Water Resour.* **25**, 861–884. https://doi.org/10.1016/S0309-1708(02)00042-8 (2002).
7. Viswanathan, H. S. et al. From fluid flow to coupled processes in fractured rock: Recent advances and new frontiers. *Rev. Geophys.* **60** https://doi.org/10.1029/2021RG000744 (2022). e2021RG000744, doi.
8. Kottwitz, M. O., Popov, A. A., Abe, S. & Kaus, B. J. Investigating the effects of intersection flow localization in equivalent-continuum-based upscaling of flow in discrete fracture networks. *Solid Earth*. **12**, 2235–2254. https://doi.org/10.5194/se-12-2235-2021 (2021).
9. Ozkaya, S. I. & Mattner, J. Fracture connectivity from fracture intersections in borehole image logs. *Comput. Geosci.* **29**, 143–153. https://doi.org/10.1016/S0098-3004(02)00113-9 (2003).
10. Huang, N., Jiang, Y., Li, B. & Liu, R. A numerical method for simulating fluid flow through 3-D fracture networks. *J. Nat. Gas Sci. Eng.* **33**, 1271–1281. https://doi.org/10.1016/j.jngse.2016.06.072 (2016).
11. Zhang, Q., Dong, S., Liu, Y., Huang, J. & Xiong, F. Algorithmic approach to discrete fracture network flow modeling in consideration of realistic connections in large-scale fracture networks. *J. Rock Mech. Geotech. Eng.* **16**, 3798–3811. https://doi.org/10.1016/j.jrmge.2024.02.011 (2024).
12. Li, W. et al. A novel approach of two-dimensional representation of rock fracture network characterization and connectivity analysis. *J. Petrol. Sci. Eng.* **184**, 106507. https://doi.org/10.1016/j.petrol.2019.106507 (2020).
13. Jing, L., Min, K. B., Baghbanan, A. & Zhao, Z. in *ISRM International Symposium-Asian Rock Mechanics Symposium.* ISRM-ARMS7-2012-2005 (ISRM).
14. Liu, R., Li, B., Jiang, Y., Huang, N. & Review Mathematical expressions for estimating equivalent permeability of rock fracture networks. *Hydrogeol. J.* **24**, 1623–1649. https://doi.org/10.1007/s10040-016-1441-8 (2016).
15. Park, Y. J., de Dreuzy, J. R., Lee, K. K. & Berkowitz, B. Transport and intersection mixing in random fracture networks with power law length distributions. *Water Resour. Res.* **37**, 2493–2501. https://doi.org/10.1029/2000WR000131 (2001).
16. von Planta, C. et al. Modelling of hydro-mechanical processes in heterogeneous fracture intersections using a fictitious domain method with variational transfer operators. *Comput. GeoSci.* **24**, 1799–1814. https://doi.org/10.1007/s10596-020-09936-7 (2020).
17. Sarkar, S., Toksoz, M. N. & Burns, D. R. *Fluid flow modeling in fractures* (Massachusetts Institute of Technology. Earth Resources Laboratory, 2004).
18. Berg, C. F. Permeability description by characteristic length, tortuosity, constriction and porosity. *Transp. Porous Media*. **103**, 381–400. https://doi.org/10.1007/s11242-014-0307-6 (2014).
19. Goli, S., Saha, S. K. & Agrawal, A. Three-dimensional numerical study of flow physics of single-phase laminar flow through diamond (diverging–converging) microchannel. *SN Appl. Sci.* **1**, 1353. https://doi.org/10.1007/s42452-019-1379-2 (2019).
20. Goli, S., Saha, S. K. & Agrawal, A. Physics of fluid flow in an hourglass (converging–diverging) microchannel. *Phys. Fluids*. **34**, 052006. https://doi.org/10.1063/5.0090190 (2022).
21. Brook, M. *Geomechanical behaviour and deformation of coal mine roof strata around faults: toward an engineering geological model* (University of New South Wales, 2016).
22. Gale, W. SCT Operations, Australia, NSW, Australia,. Review of the hydraulic conductivity and geotechnical characteristics of the overburden at Tahmoor South. Report No. TAH4083, 1-274 (2013).
23. Seers, T. D. & Hodgetts, D. Extraction of three-dimensional fracture trace maps from calibrated image sequences. *Geosphere* **12**, 1323–1340. https://doi.org/10.1130/GES01276.1 (2016).
24. Mauldon, M. Estimating mean fracture trace length and density from observations in convex windows. *Rock. Mech. Rock. Eng.* **31**, 201–216. https://doi.org/10.1007/s006030050021 (1998).

25. Chen, M. et al. Assessment of factors and mechanism contributing to groundwater depressurisation due to longwall mining. *Int. J. Coal Sci. Technol.* **11**, 1–36. https://doi.org/10.1007/s40789-024-00716-7 (2024).
26. Chen, M., Zhang, C., Canbulat, I. & Saydam, S. A DEM-DFN method for assessing mining-induced continuous fracturing and fracture connectivity in rock masses. *Rock. Mech. Rock. Eng.* 1–24. https://doi.org/10.1007/s00603-025-04658-7 (2025).
27. Jin, Y. et al. Risk analysis of natural hydraulic fracturing in an overpressured basin with mud diapirs: A case study from the Yinggehai Basin, South China sea. *J. Petrol. Sci. Eng.* **196**, 107621. https://doi.org/10.1016/j.petrol.2020.107621 (2021).
28. Guo, H., Adhikary, D. P. & Craig, M. S. Simulation of mine water inflow and gas emission during longwall mining. *Rock. Mech. Rock. Eng.* **42**, 25–51. https://doi.org/10.1007/s00603-008-0168-9 (2008).
29. Hamm, S. Y. et al. Relationship between hydraulic conductivity and fracture properties estimated from packer tests and borehole data in a fractured granite. *Eng. Geol.* **92**, 73–87. https://doi.org/10.1016/j.enggeo.2007.03.010 (2007).
30. Jones, B. R., Van Rooy, J. L. & Dippenaar, M. A. Lugeon tests at partial saturation: experimental and empirical contributions. *Rock. Mech. Rock. Eng.* **52**, 351–372. https://doi.org/10.1007/s00603-018-1592-0 (2019).
31. Bai, Q. & Tu, S. A general review on longwall mining-induced fractures in near-face regions. *Geofluids* 1–22, (2019). https://doi.org/10.1155/2019/3089292 (2019).
32. Kowalski, A. C. G., Mendonça, C. A. & Ofterdinger, U. S. Fracture flow characterization with low-noise spontaneous potential logging. *Groundwater* **59**, 16–23. https://doi.org/10.1111/gwat.13009 (2021).
33. Quinn, P. M., Cherry, J. A. & Parker, B. L. Quantification of non-Darcian flow observed during packer testing in fractured sedimentary rock. *Water Resour. Res.* **47**, W09533. https://doi.org/10.1029/2010WR009681 (2011).
34. Xiong, W., Shen, K., Ba, Q., Liu, Y. & Zhou, H. A liquid-solid model to optimize the application of friction reducers for hydraulic fracturing/cutting in the underground coal mine. *Energy Sci. Eng.* **9**, 1568–1582. https://doi.org/10.1002/ese3.930 (2021).
35. Zhang, Y., Chai, J., Cao, C. & Shang, T. Combined influences of shear displacement, roughness, and pressure gradient on nonlinear flow in self-affine fractures. *J. Petrol. Sci. Eng.* **198**, 108229. https://doi.org/10.1016/j.petrol.2020.108229 (2021).
36. Li, B., Liu, R. & Jiang, Y. Influences of hydraulic gradient, surface roughness, intersecting angle, and scale effect on nonlinear flow behavior at single fracture intersections. *J. Hydrol.* **538**, 440–453. https://doi.org/10.1016/j.jhydrol.2016.04.053 (2016).
37. Liu, R., Jiang, Y. & Li, B. Effects of intersection and dead-end of fractures on nonlinear flow and particle transport in rock fracture networks. *Geosci. J.* **20**, 415–426. https://doi.org/10.1007/s12303-015-0057-7 (2016).
38. Chen, M., Zhang, C., Canbulat, I. & Saydam, S. Assessment of groundwater depressurisation due to mining considering flow nonlinearity in connected fractures. *Rock. Mech. Rock. Eng.* **58**, 4347–4376. https://doi.org/10.1007/s00603-025-04434-7 (2025).

## Figures

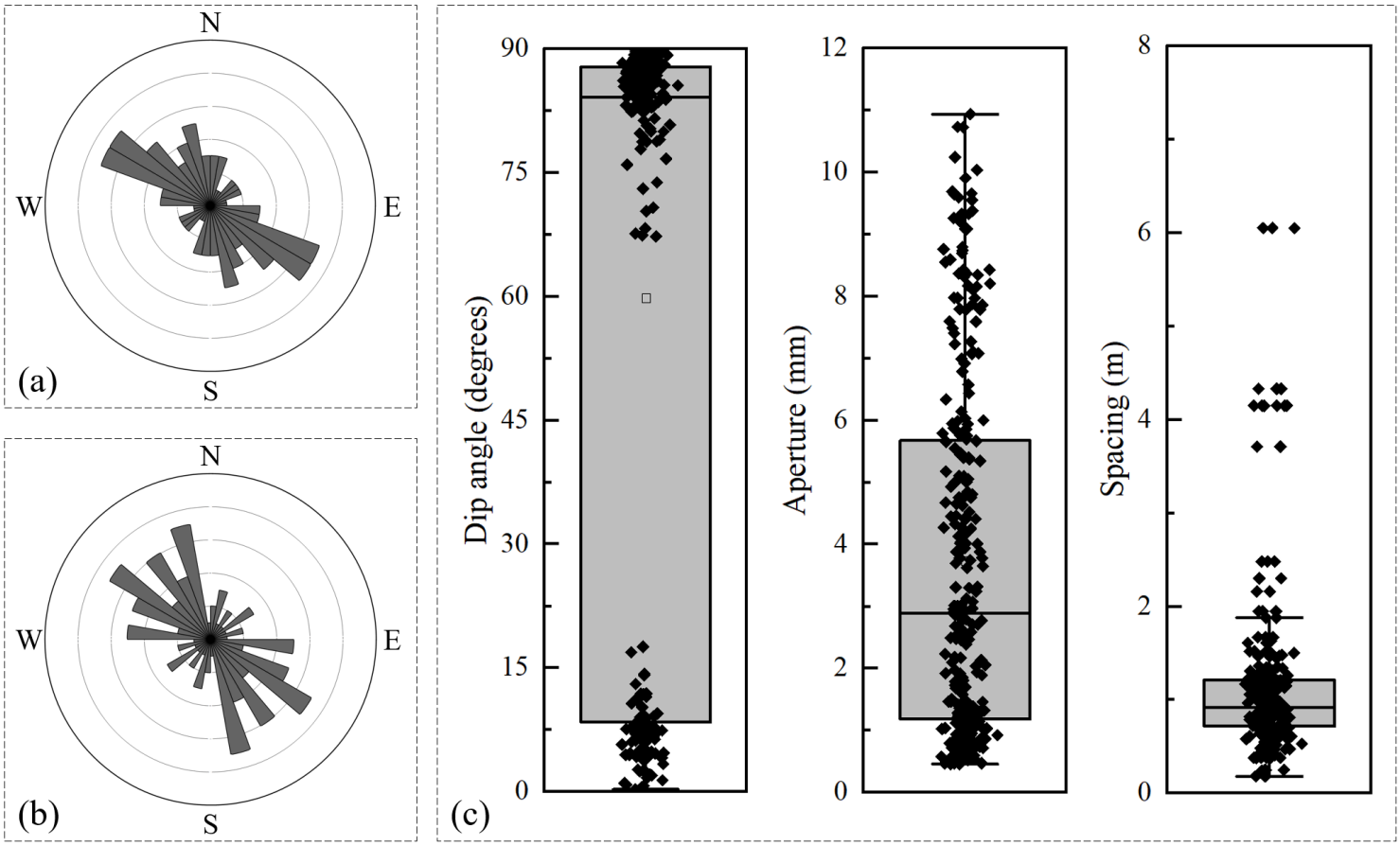



**Figure 1**

Rosette plots of fractures derived from borehole (**a**) BH1 and (**b**) BH2, accompanied by (**c**) statistical analyses in terms of dip angle, aperture, and spacing.

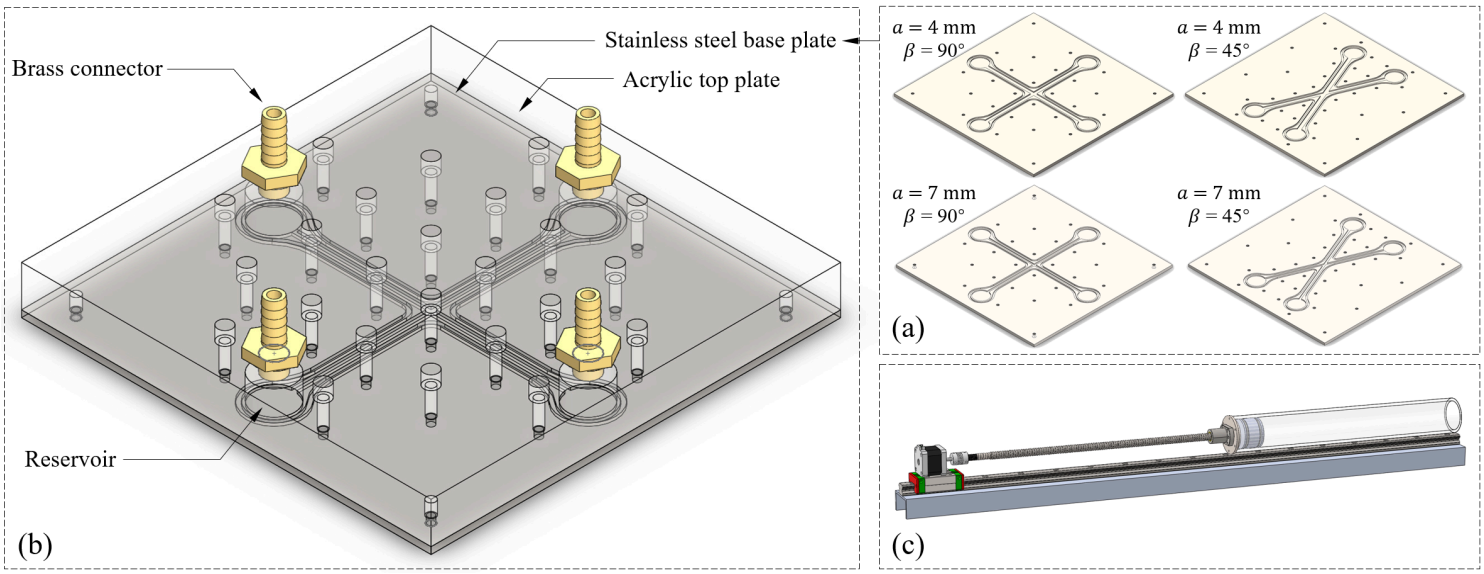



**Figure 2**

Schematic of the experimental system: (**a**) flow pathways with varying apertures and intersection angles, (**b**) overall configuration of the flow chambers, and (**c**) syringe pump units.

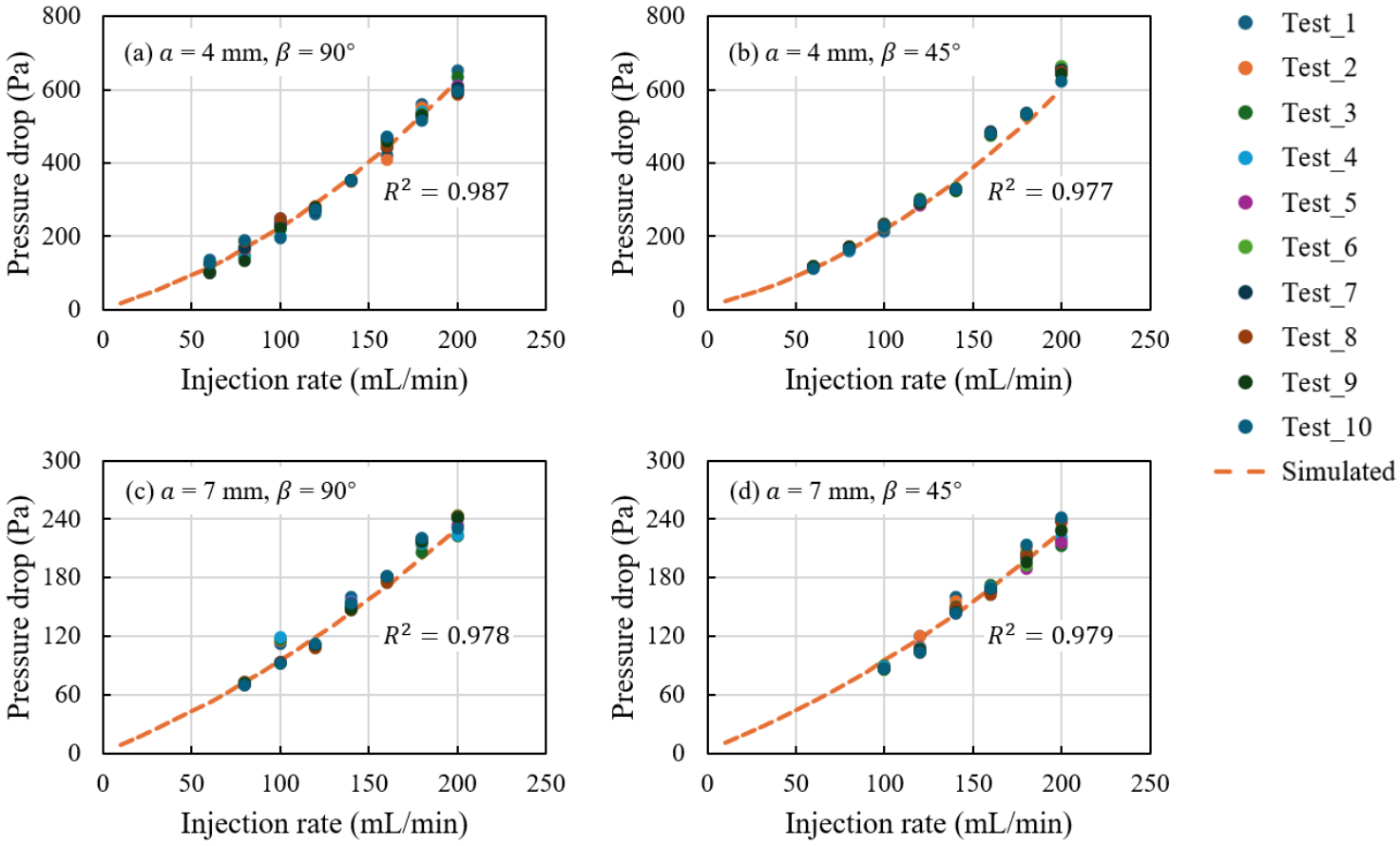



**Figure 3**

Numerical model calibration for (**a**) aperture of 4 mm and dip angle of 90 degrees, (**b**) aperture of 4 mm and dip angle of 45 degrees, (**c**) aperture of 7 mm and dip angle of 90 degrees, and (**d**) aperture of 7 mm and dip angle of 45 degrees.

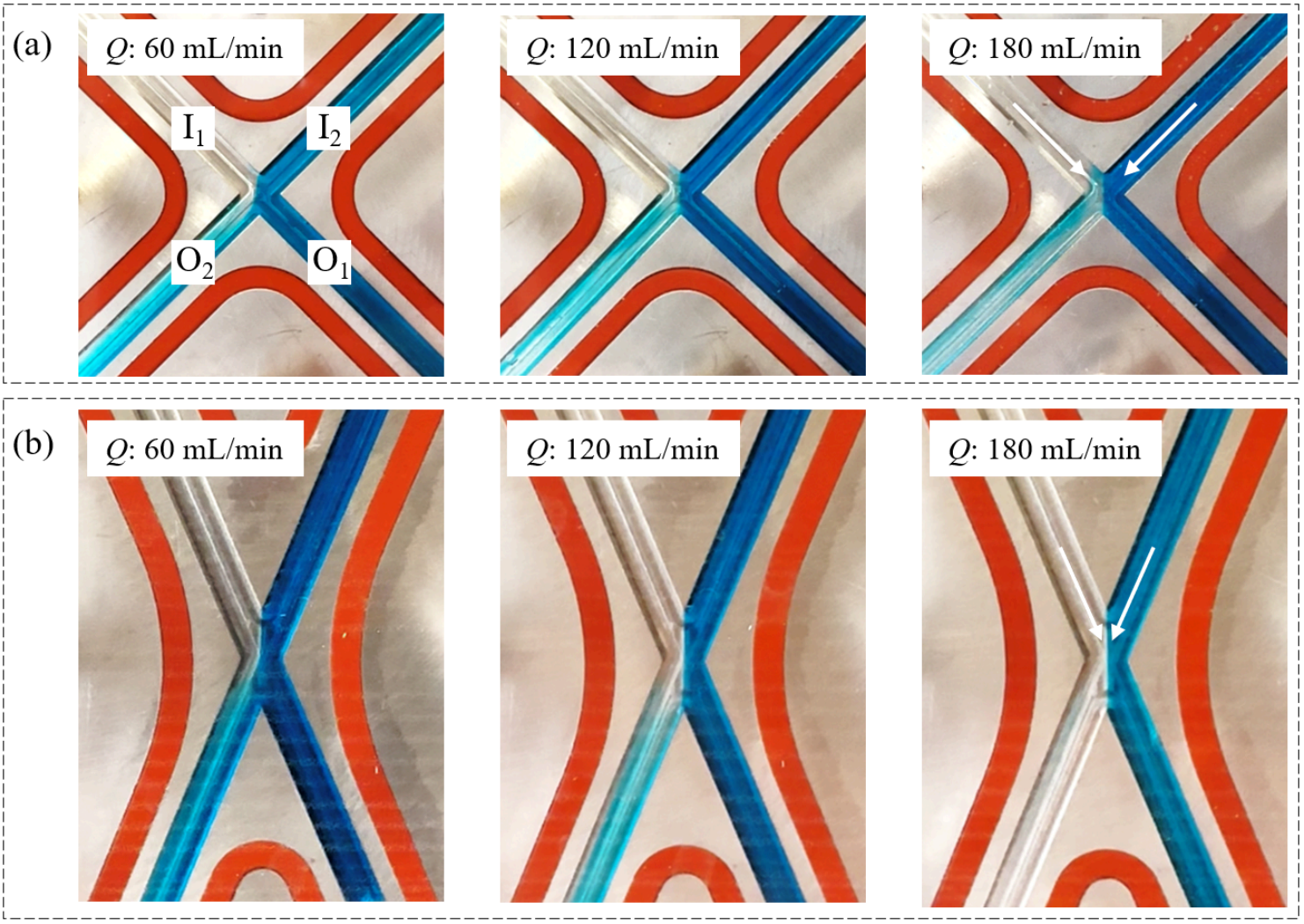



**Figure 4**

Fluid flow tests for dip angles of (**a**) 90 degrees and (**b**) 45 degrees [38].

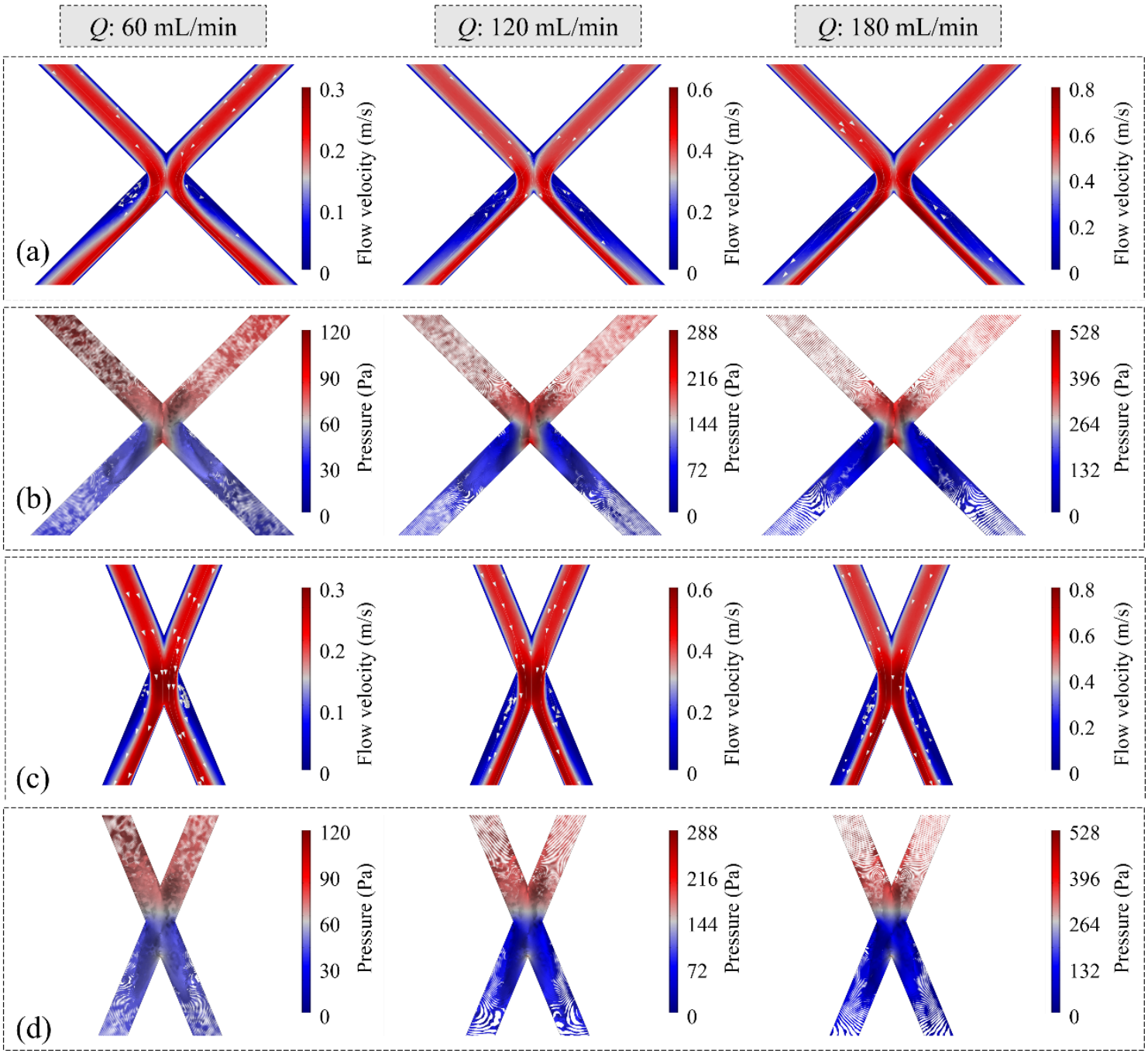



**Figure 5**

Velocity magnitude and pressure under (**a-b**) 90-degree intersection and (**c-d**) 45-degree intersection conditions.

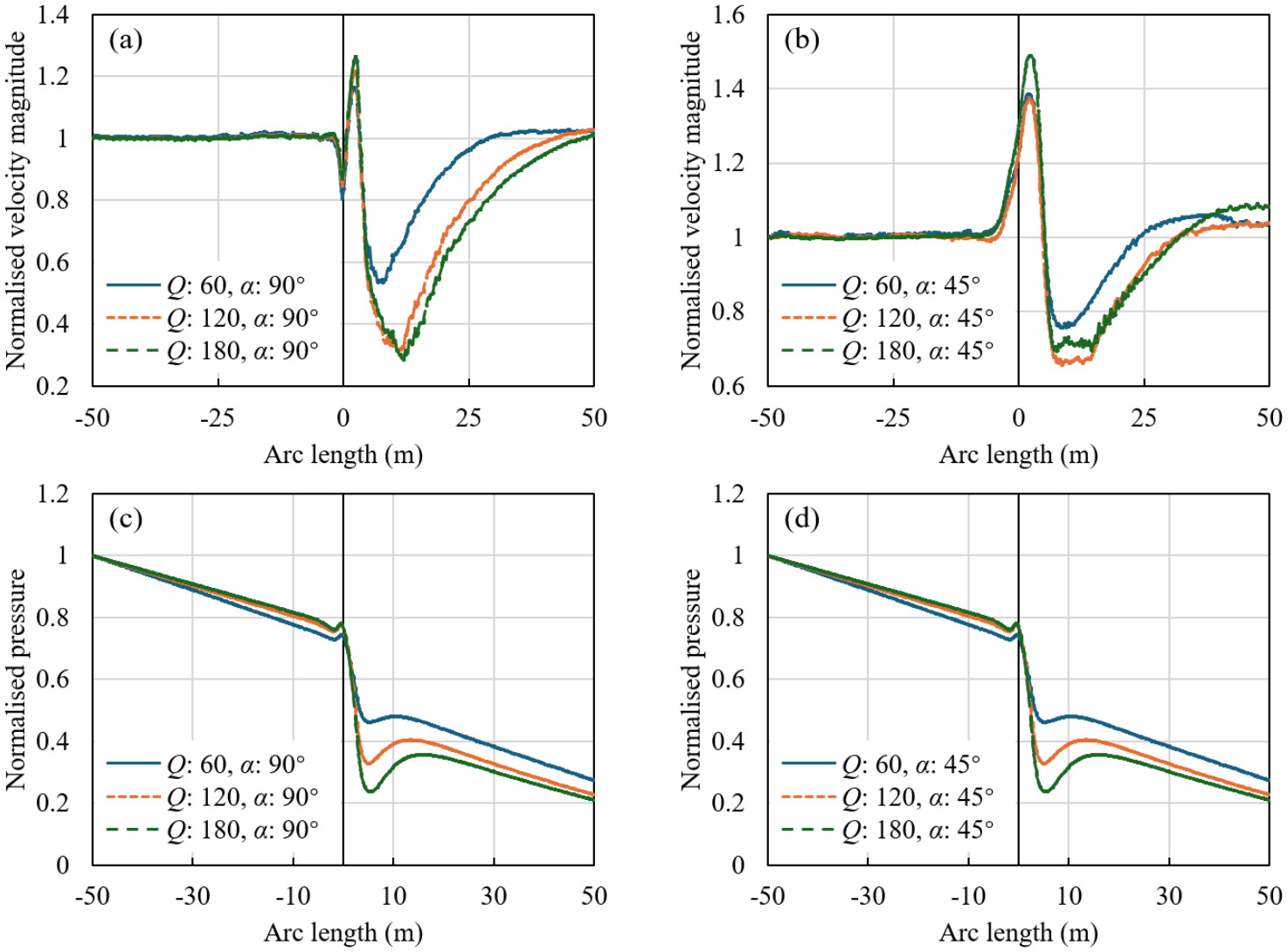



**Figure 6**

Quantitative assessments of (**a-b**) normalised flow velocity magnitude and (**c-d**) normalised pressure at different injection rates and intersection angles.

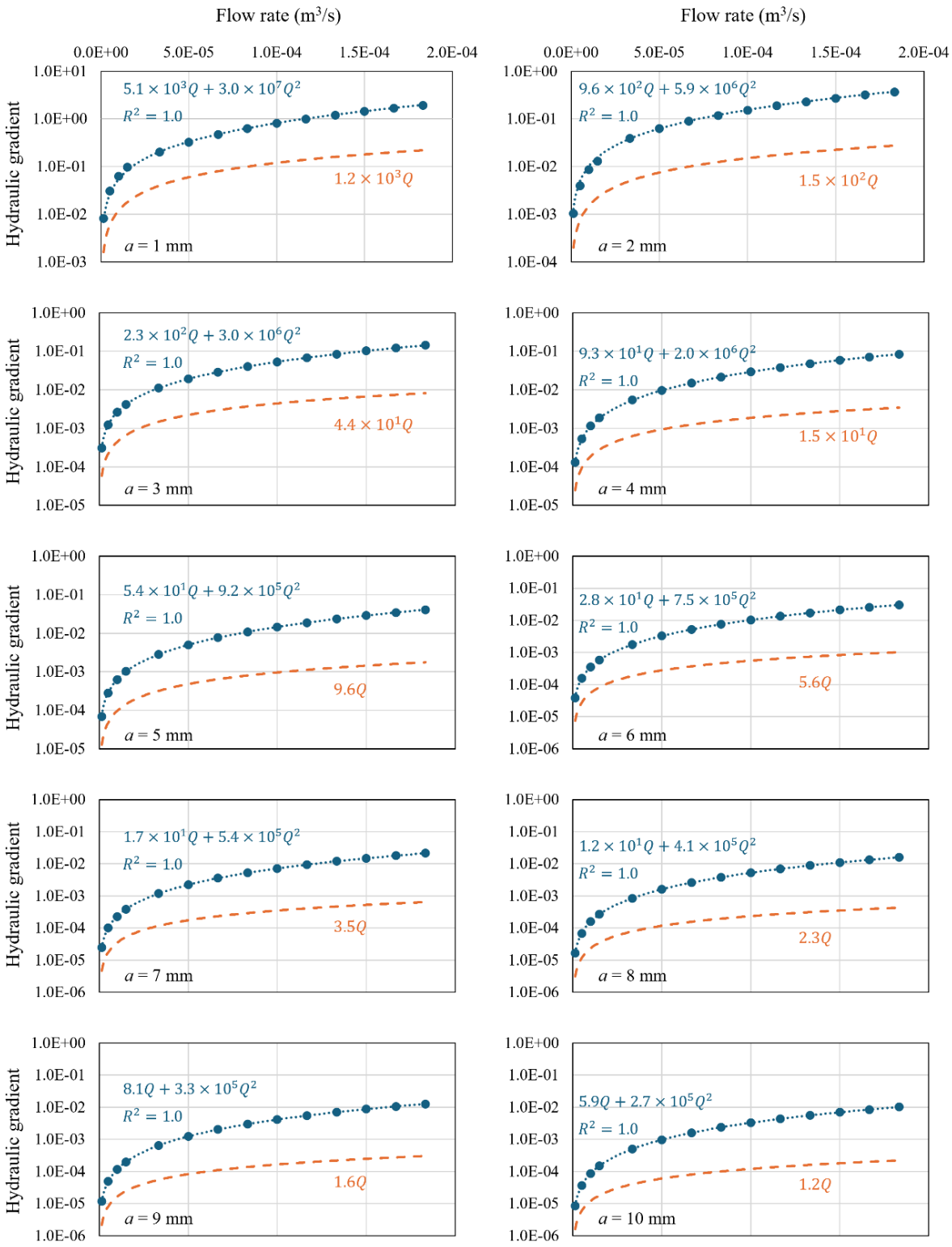



**Figure 7**

Comparison of linear and power-law relationships between hydraulic gradient and flow rate under different apertures (α).

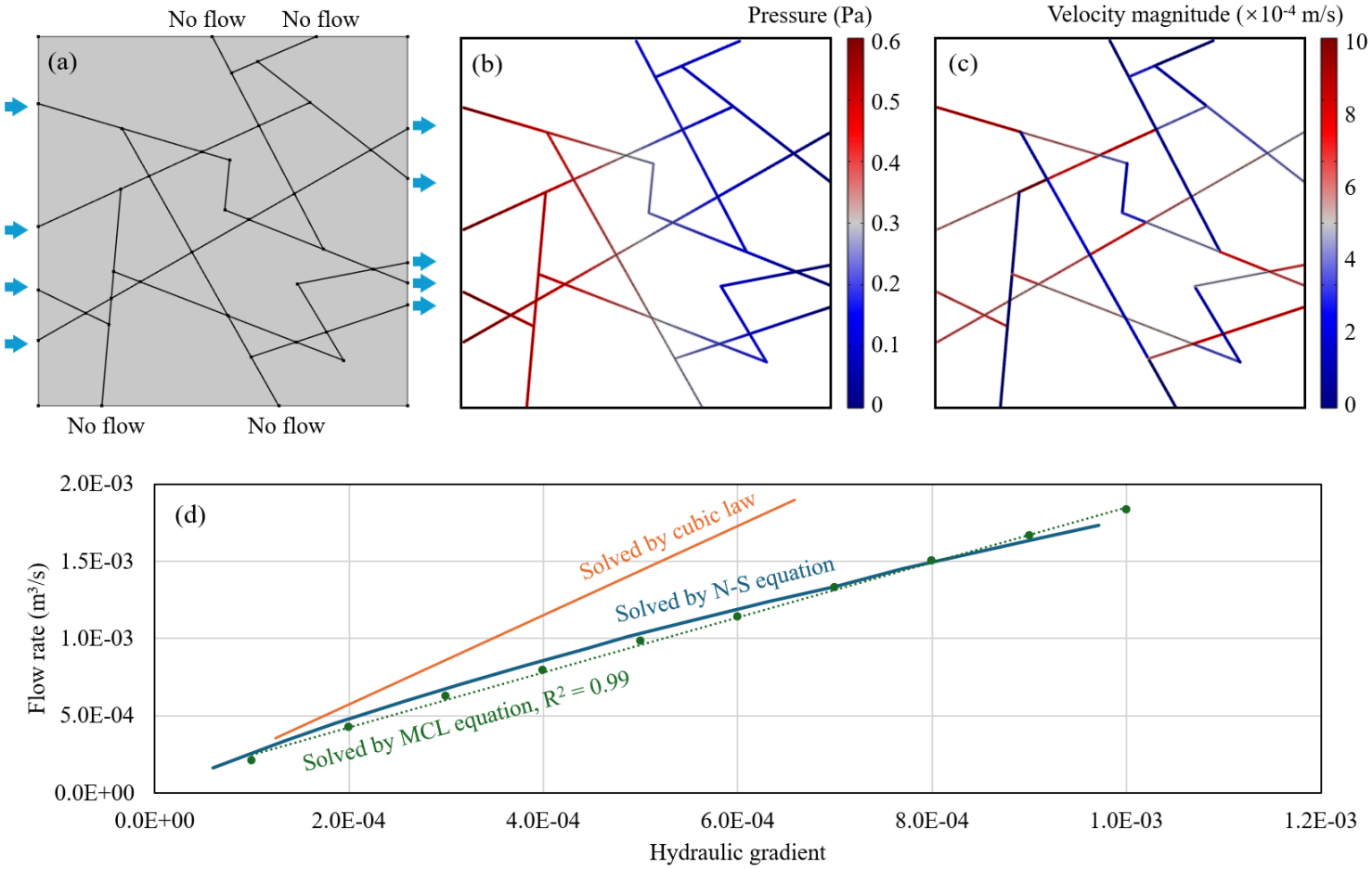



**Figure 8**

Validation of the modified cubic law (MCL) (Eq. 9). (**a**) Fracture network developed in COMSOL. (**b-c**) Distributions of fluid pressure and velocity magnitude under a hydraulic gradient of $6\times10^{-5}$. (**d**) Comparison of flow rates predicted by the cubic law, MCL, and N-S equations.